

1. Fundamentals

1.1 Introduction

At room temperature, an object emits most of its energy in the form of infrared radiation. Therefore, in observing terrestrial objects and activities without light reflection, infrared radiation is one of the most important spectrum to be monitored. However, finding a suitable material for infrared detection is always a challenge. In order to detect radiation of a particular energy, compound semiconductors with various bandgaps have to be sought in order to create desirable optical absorption. Problems arise if the material is unstable, nonuniform or not semi-insulating. In such cases, light detection capability will be greatly compromised.

Photoconductivity of a semiconductor is a classical branch of physics. The underlying physical principles have been thoroughly studied over the years. The detector structures, usually in the form of a photodiode, are also well established. Therefore, the improvement of detector performance usually relies on the improvement of material quality rather than the detector design. The research in infrared photodetectors in the present days is better characterized as a branch of material science rather than a branch of physics. It is particularly true for the more difficult detector materials such as HgCdTe. For these materials, a better understanding of the correlation between the material preparation procedures and the resulting detector properties is more essential in improving the detector performance.

The situation is quite different for the more recently developed quantum well infrared photodetectors (QWIP). These detectors are based on the optical transition within a single energy band and are therefore independent on the bandgap of the detecting material. Based on the new detector concept, a material can be used to detect a much lower energy radiation than what is allowed by the separation between its valence band and the conduction band. The choice of detector material is thus substantially widen, and in most case, the conventional material can be substituted by a more matured and better behaved material system. In QWIPs, infrared absorption occurs via intersubband transitions. The transition energy is determined by the energy levels in each quantum well, and can be varied by changing its structure. A good example is that made of GaAs/Al_xGa_{1-x}As. Since GaAs material technology is well established, detector performance is not significantly limited by its material quality but rather by the intrinsic opto-electronic properties of the QWIP. Therefore, in order to improve the detector performance, it is more important in this case to better understand the basic detector

physics.

Different from a bulk semiconductor in which the material properties are fixed by nature, a QWIP consists of an artificial material structure whose parameters can be practically assigned at will. Since there are unlimited combinations of different material parameters, actually, there are no definitive QWIP structures that are suitable for all applications. An optimized detector structure depends on a number of factors, including the source spectrum, the temperature of operation, the characteristics of readout electronics, the light coupling scheme and the material preparation conditions. The task of QWIP research is to find the best combination of material parameters for a particular application.

The purpose of this book is to give a detailed and more systematic description on the basic operating principles of QWIPs. In this chapter, some fundamentals will be given in relation to infrared detection. In chapter 2, different methods will be discussed in calculating the energy levels in quantum wells. In chapter 3, the effects of a crystal lattice on the quantum well properties will be discussed. In chapter 4, the changes of the energy levels in the presence of many-body interactions will be described. In chapter 5, the absorption energy and the absorption lineshape of intersubband transition in various quantum well structure will be discussed. In chapter 6, different optical coupling schemes will be presented.

In chapter 7, a related device structure, which is known as a hot-electron transistor, will be introduced. It is one of the building blocks for the infrared hot-electron transistor (IHET). To study the electron transport properties of a QWIP, it is informative to know the energy distribution of the electrons in the structure. For this reason, in chapter 8, two characterization techniques are introduced, which are known as thermally and optically stimulated hot-electron spectroscopies. From these studies, the intrinsic optoelectronic properties of a QWIP as well as the extrinsic material properties can be much better understood. The transport properties of a QWIP will be discussed in chapter 9.

In chapter 10, the photoconductivity and the noise properties of QWIPs will be discussed, and in chapter 11, the advantages in converting a QWIP into an IHET are presented. It turns out that the same device structure used in excitation hot-electron spectroscopy is not only useful in the basic studies, but is also able to improve the detector performance. To name a few, it increases the detectivity of a QWIP, amplifies a photovoltage, and reduces noise. Noise in the quantum structures is an interesting subject. It is especially true for an IHET, which has three terminals. Noise properties of this quantum device will be discussed in chapter 12.

In addition to its versatility in the detection wavelengths, a QWIP offers new capability in infrared detection. Multi-color infrared detection is one of the examples. This feature will be discussed in chapter 13. Finally, in chapter 14, the performance of QWIP in meeting the industrial standard will be discussed.

Infrared detection is a multi-disciplinary subject. Besides a knowledge of solid state physics, a better appreciation of the art also requires the knowledge of many other subjects, including the radiation emission and transmission, modern electronic readout design, optical system design, detector noise and system noise, and application requirements. A successful detector design can be realized only when all these factors are taken into account. In fact, it is impossible to specify the detector figures of merit without reference to a particular readout design or application. Although this book is devoted to the physics of QWIPs, it is the author's hope that the reader will get some flavor from each subject to prepare for a more advanced study.

We should point out that the study of QWIPs and IHETs is not necessarily motivated by their potential applications. In these structures, some of the fundamental quantum phenomena, such as energy quantization in a box, quantum mechanical transmission and the simplest case of dipole transition, are magnificently displayed. They can serve as the classical examples for elementary quantum mechanics. Another exciting feature of this subject is that one can actually design a structure for a particular quantum phenomenon to or not to occur, instead of passively observing what is given by nature. The fascination of the subject is then only limited by one's imagination.

In addition, these devices offer unique band structures and well controlled material parameters, with which many physical phenomena can be better displayed and quantitatively understood. For example, using multiple quantum well MQW structures, resonant tunneling is more pronounced because of the 2-dimensional density of states of the quantum wells. By exciting electrons with thermal or optical energies, electron transport can be studied as a function of electron energy in addition to applied biases. Using a monochromatic light source, an electron can be placed in a MQW at a specific energy. This ability creates a new degree of freedom in studying a number of physical processes such as hot-electron dynamics, electron energy relaxation, and impact-ionization.

With an IHET structure, the hot-electrons generated in a QWIP can also be used to study electron energy relaxation in the base which is made of bulk materials or used to probe the band structure of another quantum well structure placed at the collector. It is also valuable in determining the energy distribution of detector dark current,

photocurrent and noise current, and in creating a system to study the noise of quantum particles. Using the optical absorption spectroscopy and infrared photoelectron tunneling spectroscopy described in this book, one can study material parameters such as band offset, band nonparabolicity, miniband structures of quantum wells, coherence of electron wave function and interwell electron coupling etc. Therefore, QWIPs and IHETs are not only useful for infrared detection but also useful for fundamental studies.

1.2 Blackbody radiation and flux transfer

Infrared detectors are used to detect radiation emitted by a target. The intensity of the radiation is determined by a number of factors such as the target temperature, the distance and the size of the target as well as its emissivity. Besides the source intensity, the optical signal received by a detector is also dependent on the transmission of the medium and the optical design of the detector system. In section 1.2.1, the radiation from a blackbody will be reviewed. In section 1.2.2, the flux received by a detector under a simple optical system will be discussed.

1.2.1 Blackbody radiation

Assuming the emissivity of the object to be unity as it would be for a perfect blackbody, the amount of radiation emitted by that object will be determined by the absolute temperature T , and is governed by the Planck equation:

$$L(T, \lambda) = \frac{2c}{\lambda^4} \frac{1}{e^{hc/\lambda kT} - 1}, \quad \left[\frac{ph}{s} \frac{1}{cm^2} \frac{1}{sr} \frac{1}{\mu m} \right] \quad (1.1)$$

where $L(T, \lambda)$ is the spectral radiance, defined as the photon flux per unit projected area per unit solid angle per unit wavelength. In Eq. (1.1), λ is the wavelength, $h = 6.6262 \times 10^{-34}$ Js is the Planck's constant, $c = 2.9979 \times 10^8$ m/s is the speed of light *in vacuo*, $k = 1.3806 \times 10^{-23}$ J/K is the Boltzmann constant. If the radiation is Lambertian *ie.* isotropic, the spectral exitance in a cone of half-angle θ , $M_\theta(T, \lambda)$, of a circularly symmetric system, is given by

$$M_{\theta}(T, \lambda) = \int_0^{\theta} \int_0^{2\pi} L(T, \lambda) \sin \theta \cos \theta d\phi d\theta, \quad \left[\frac{ph}{s} \frac{1}{cm^2} \frac{1}{\mu m} \right] \quad (1.2)$$

$$= L(T, \lambda) \pi \sin^2 \theta .$$

The exitance, $M(T, \lambda)$, into the entire hemisphere can be obtained by setting $\theta = 90^\circ$.

$$M(T, \lambda) = \pi L(T, \lambda) . \quad \left[\frac{ph}{s} \frac{1}{cm^2} \frac{1}{\mu m} \right] \quad (1.3)$$

Fig. 1.1 shows $M(T, \lambda)$ at different temperatures and wavelengths. The wavelength λ_{max}

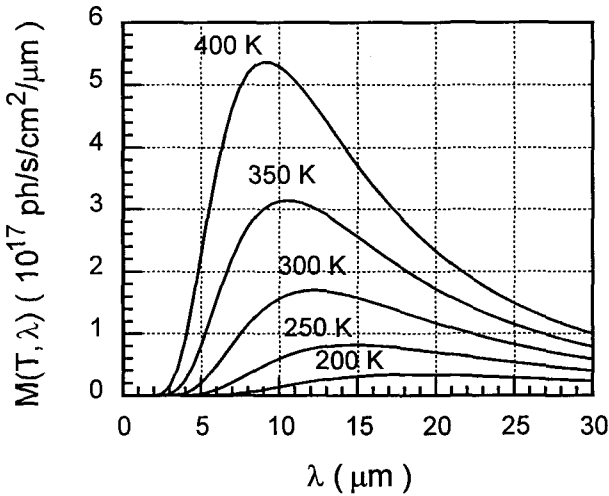


Fig. 1.1 The exitance of a blackbody as a function of wavelength at different temperatures

at the peak of radiation can be obtained by setting $dM(T, \lambda)/d\lambda = 0$, which gives

$$\lambda_{max} T = 3670 \mu m K . \quad (1.4)$$

At $T = 300 K$, $\lambda_{max} = 12.2 \mu m$. The total photon flux emitted by a blackbody is

6 1. Fundamentals

$$\begin{aligned}
 M &= \int_0^{\infty} M(T, \lambda) d\lambda, \\
 &= \frac{4 \pi k^3 T^3}{c^2 h^3} \text{Zeta}(3), \quad \left[\frac{ph}{s \text{ cm}^2} \right] \\
 &= 1.52023 \times 10^{11} T^3.
 \end{aligned} \tag{1.5}$$

For $T = 300 \text{ K}$, $M = 4.105 \times 10^{18} \text{ ph/s/cm}^2$. For thermal imaging, there are two atmospheric windows of interest. One is located at 3 to 5 μm band, another is at 8 to 12 μm band. The exitance, $M(T, \lambda_1, \lambda_2)$, between two wavelengths λ_1 and λ_2 is given by

$$\begin{aligned}
 M(T, \lambda_1, \lambda_2) &= \int_{\lambda_1}^{\lambda_2} M(T, \lambda) d\lambda, \\
 &= 6.3235 \times 10^{11} T^3 \int_{x_2}^{x_1} \frac{x^2 dx}{e^x - 1}, \quad \left[\frac{ph}{s \text{ cm}^2} \right]
 \end{aligned} \tag{1.6}$$

where $x \equiv hc/kT\lambda$. Fig. 1.2 shows $M(T, \lambda_1, \lambda_2)$ at different temperatures for two wavelength ranges, 3 to 5 μm and 8 to 10 μm .

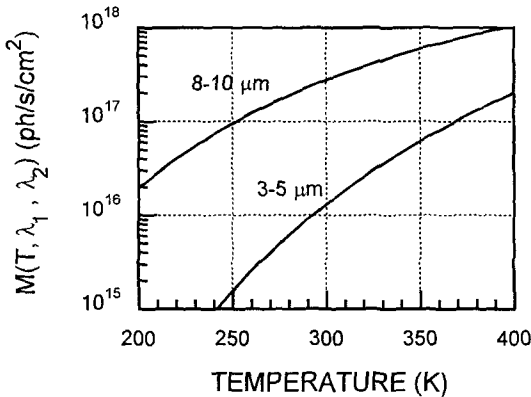


Fig. 1.2 The exitance between 3 to 5 μm and 8 to 10 μm as a function of temperature.

At 300 K, the photon flux between 8 to 10 μm is 2.771×10^{17} ph/s/cm², which is 6.75 % of the total photon flux emitted by the blackbody, and is a factor of 21.1 larger than that emitted between the 3 to 5 μm . The higher intensity of radiation emitted at the 8 to 10 μm range argues for infrared detection at this wavelength range. A room temperature object will be brighter in these wavelengths, and hence is easier to detect. It is even more so for temperatures lower than 300 K where the difference between the two photon fluxes is even larger. On the other hand, the shorter wavelength curve in Fig. 1.2 has a steeper slope. At $T = 643$ K, the two curves eventually intercept each other, beyond which, the 3 to 5 μm radiation becomes more intense. A shorter wavelength detector is therefore more suitable to detect objects at the higher temperature range.

When the intensity of the target is sufficient, the larger temperature dependence of $M(T, 3 \mu\text{m}, 5 \mu\text{m})$ offers an advantage in thermal imaging. When the background of the scene is at a similar temperature as the target, the identification of the target depends on the contrast between the target and the scene. In this case, $\partial M(T, \lambda_1, \lambda_2)/\partial T$ is a more important quantity. Assuming the photon energy hc/λ much larger than the thermal energy kT ,

$$\begin{aligned} \frac{\partial M(T, \lambda_1, \lambda_2)}{\partial T} &= \frac{\partial}{\partial T} \int_{\lambda_1}^{\lambda_2} \frac{2 \pi c}{\lambda^4} e^{-hc/\lambda k T} d\lambda, \\ &= \int_{\lambda_1}^{\lambda_2} \frac{2 \pi c}{\lambda^4} e^{-hc/\lambda k T} \frac{hc}{\lambda k T^2} d\lambda, \left[\frac{ph}{s} \frac{1}{\text{cm}^2} \frac{1}{K} \right] \quad (1.7) \\ &= \frac{hc}{\lambda k T^2} M(T, \lambda_1, \lambda_2), \end{aligned}$$

where $\bar{\lambda}$ is the average wavelength. Hence, if one defines the contrast C to be $\Delta M/M$ when ΔT is 1 K, then

$$C = \frac{hc}{\lambda k T^2}. \quad (1.8)$$

For $\bar{\lambda} = 9 \mu\text{m}$, $C = 0.0178$, and when $\bar{\lambda} = 4 \mu\text{m}$, $C = 0.040$ at $T = 300$ K. Therefore, the contrast of a given scene will appear to be twice as large when it is observed in the 3 to 5 μm range than in the 8 to 10 μm range. Fig. 1.3 shows the contrast at different scene temperature.

Other than the source characteristics, the transmission of the infrared radiation through the atmosphere also plays an important role in long range infrared detection. The common weather conditions that affect the infrared propagation are haze, rain, humidity and fog. Haze is caused by small particles suspended in the air which scatter radiation. The longer wavelength will suffer less scattering and therefore more favorable in this case. On the other hand, water vapor absorbs radiation slightly stronger in the 8 to 12 μm than in 3 to 5 μm . Therefore, in high humidity condition, the 3 to 5 μm is a better choice. In the cases of rain or fog, the radiation in the two infrared regimes attenuate equally because it is caused by a combination of scattering and absorption. In a sunny day, reflection of sun light in the 3 to 5 μm will affect detection in these wavelengths more adversely.

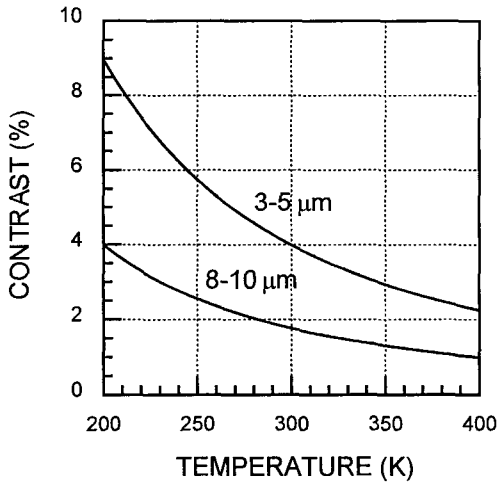


Fig. 1.3 The contrast of the scene detected at the two wavelength ranges.

1.2.2 Flux transfer

Assuming the source radiation to be isotropic, the radiation will be directly proportional to the projected solid angle Ω of the source as shown in Fig. 1.4. It is related to a cone of half-angle θ by

$$\begin{aligned}\Omega &= \int_0^{2\pi} \int_0^\theta \sin \theta \cos \theta \, d\theta, \\ & \quad [sr] \end{aligned} \quad (1.9)$$

$$= \pi \sin^2 \theta .$$

In contrast, the solid angle ω is equal to

$$\begin{aligned}\omega &= \int_0^{2\pi} \int_0^\theta \sin \theta \, d\theta \, d\phi, \\ & \quad [sr] \end{aligned} \quad (1.10)$$

$$= 2\pi (1 - \cos \theta) .$$

For a full hemisphere ($\theta = 90^\circ$), $\omega = 2\pi$ which is one-half of the area of a unit sphere, whereas $\Omega = \pi$ is the area of the base of a unit sphere as shown in Fig. 1.4.

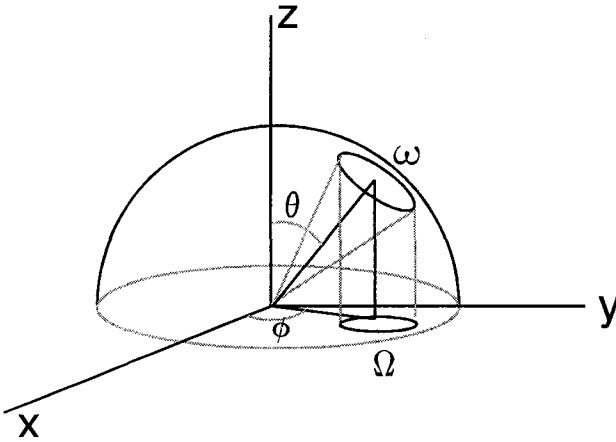


Fig. 1.4 The relation between the solid angle ω and the projected solid angle Ω .

Now consider two disks, D_1 and D_2 , with areas A_1 and A_2 separated at a distance s from their centers such that s is much larger than the linear dimensions of D_1 and D_2 . Their spatial orientations are illustrated in Fig. 1.5. The first disk may represent the

radiation source, and the second one represents the detector. In this case, the flux Φ radiated by D_1 and entered into D_2 is given by

$$\begin{aligned}
 \Phi &= \int_{\lambda} \int_{A_1} \int_{\omega_1} L(\lambda) \cos \theta_1 d\omega_1 dA_1 d\lambda, \\
 &= \left(\int_{\lambda} L(\lambda) d\lambda \right) \left(\cos \alpha_1 \int_{A_1} dA_1 \right) \left(\int_{\omega_1} d\omega_1 \right), \\
 &= LA_1 (\cos \alpha_1) \omega_1, \qquad \qquad \qquad [ph/s] \qquad \qquad (1.11) \\
 &= LA_1 \cos \alpha_1 \frac{A_2 \cos \alpha_2}{s^2}, \\
 &= L \frac{A_1 \cos \alpha_1}{s^2} A_2 \cos \alpha_2.
 \end{aligned}$$

In Eq. (1.11), L is the shorthand for $L(T, \lambda_1, \lambda_2) = M(T, \lambda_1, \lambda_2)/\pi$, and we have

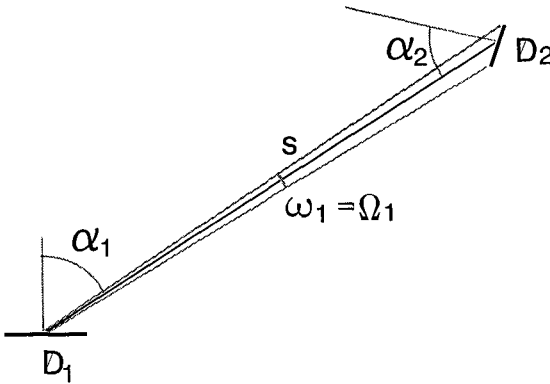


Fig. 1.5 The orientations of two circular disks.

assumed the variable θ_1 is approximately constant and is equal to α_1 . ω_1 is the solid angle of D_2 sustained on D_1 , since A_2 is not normal to the line of sight at D_1 , ω_1 is given by $A_2 \cos \alpha_2 / s^2$, and is equal to the projected solid angle Ω_1 of D_2 on D_1 . The last step of Eq. (1.11) emphasizes the symmetry of the expression between the two disks, it can be

arrived by considering the radiation received at D_2 instead of considering the radiation emitted by D_1 . We therefore define a quantity, which is known as the throughput Υ of an optical system,

$$\Upsilon = A_p \Omega , \quad [cm^2 sr] \tag{1.12}$$

where A_p is the projected area and Ω is the projected solid angle. Apparently, from Eq. (1.11), Υ can be calculated at D_1 or D_2 .

Now, let us consider two common optical systems as illustrated in Fig. 1.6. Fig. 1.6(a) shows a detector D_2 facing an extended light source. The field of view FOV, characterized by the half-cone angle θ , is limited by a field stop D_1 , $D_1 \gg D_2$. The flux Φ received by the detector is

$$\begin{aligned} \Phi &= L \Upsilon , \\ &= L A_d \pi \sin^2 \theta . \end{aligned} \quad [ph/s] \tag{1.13}$$

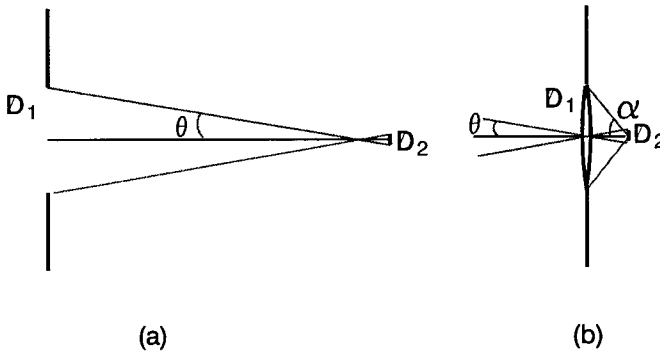


Fig.1.6 (a) A typical arrangement of a detector and a field stop, and (b) a typical arrangement of a detector and a lens.

Now, if a lens is installed at the field stop as shown in Fig. 1.6(b), the detector can be moved toward the lens and placed at the focal length f of the lens. The lens increases the

throughput of the system, and the flux Φ_L on the detector with the lens is

$$\Phi_L = LA_d \pi \sin^2 \alpha \cdot [ph/s] \quad (1.14)$$

Note that the field of view, which is defined by the light beams passing through the center of the lens need not be changed, and can still be equal to θ . If this is the case, $Y_L (= A_L \pi \sin^2 \theta)$ calculated at the lens should be equal to $Y_d (= A_d \pi \sin^2 \alpha)$ calculated at the detector. Eq. (1.14) becomes

$$\Phi_L = LA_L \pi \sin^2 \theta \cdot [ph/s] \quad (1.15)$$

Comparing Eq. (1.13) and Eq. (1.15), Φ_L/Φ is equal to A_L/A_d , which is expected because all the flux falling on the lens within an angle θ is focused on the detector. The flux-gathering power of an optical system is usually characterized by the f-number, F , which is defined as

$$F = \frac{1}{2 \sin \alpha} \cdot \quad (1.16)$$

Hence,

$$\Phi_L = \frac{\pi LA_d}{4F^2} = \frac{A_d M(T, \lambda_1, \lambda_2)}{4F^2} \cdot \quad (1.17)$$

The flux on the detector is seen to increase when the f-number of the lens decreases. When F is large, the usual approximation is

$$F \approx \frac{f}{D} \cdot \quad (1.18)$$

where f is the focal length and D is the diameter of the lens or the entrance aperture.

On the other hand, if the lens is removed in Fig. 1.6(b) without relocating the detector, the flux falling on the detector will remain the same since the throughput is unchanged. In this case, the effect of the lens is to reduce the field of view from α to θ and hence improving the spatial resolution of the detector without sacrificing the amount of optical flux on the detector.

1.3 Signal and noise in photodetection

In this section, we will review the basic principle of photodetection. Assuming there is a photon flux Φ_s falling on a detector which generates photoelectrons, and the average number of electrons collected in time duration τ_d is \bar{n} , then the quantum efficiency η can be defined by the following expression

$$\frac{\bar{n}}{\tau_d} \equiv \eta \Phi_s . \quad [e^-/s] \quad (1.19)$$

The photocurrent i_s measured is

$$i_s = e \frac{\bar{n}}{\tau_d} = e \eta \Phi_s , \quad (1.20)$$

where e is the magnitude of an electron charge. The generation process is assumed to be random, both due to the random arrival of photons and the spontaneous nature of the absorption process, so that the photoemission process obeys Poisson statistics. Based on this statistics, the mean-square fluctuation in n is

$$\overline{(n - \bar{n})^2} = \bar{n} , \quad (1.21)$$

and the mean-square current fluctuation is

$$i_n^2 = \overline{(i - \bar{i})^2} = \frac{e^2}{\tau_d^2} \overline{(n - \bar{n})^2} = \frac{e^2}{\tau_d^2} \bar{n} = \frac{e}{\tau_d} i_s . \quad (1.22)$$

In terms of η and Φ_s ,

$$i_n^2 = \frac{e^2}{\tau_d} \eta \Phi_s . \quad (1.23)$$

i_n is the intrinsic or the minimum noise current associated with optical detection. The signal power is larger than the noise power when $i_s^2 > i_n^2$, comparing Eq. (1.20) and Eq. (1.24) gives

$$\eta \Phi_s \tau_d = \bar{n} > 1 . \quad (1.24)$$

Eq. (1.24) stated that the signal will be larger than the noise if on the average, more than one photoelectron are collected in each sampling time. This condition is the minimum requirement to produce a dc signal. If we define the noise equivalent flux Φ_{SL} to be the signal flux with which the signal to noise level $(S/N)_p$ equals one, then in this signal-noise-limited case,

$$\Phi_{SL} = \frac{1}{\eta \tau_d} . \quad (1.25)$$

Now, we consider another case where, in addition to the photon flux from the target Φ_s , there is also flux from the background Φ_b . The noise current is then given by

$$\overline{i_n^2} = \frac{e^2}{\tau_d} \eta (\Phi_s + \Phi_b) , \quad (1.26)$$

and the noise equivalent flux NEF is

$$NEF = \frac{1}{2 \eta \tau_d} + \frac{1}{2 \eta \tau_d} \sqrt{1 + 4 \eta \tau_d \Phi_b} = \frac{\Phi_{SL}}{2} + \frac{\Phi_{SL}}{2} \sqrt{1 + 4 \frac{\Phi_b}{\Phi_{SL}}} . \quad (1.27)$$

When Φ_b is larger than Φ_{SL} , the detection is background-limited, and the corresponding noise equivalent flux Φ_{BL} is

$$\Phi_{BL} = \Phi_{SL}^{1/2} \Phi_b^{1/2} . \quad (1.28)$$

1.3.1 Optical signal of a photoconductor

Since the quantum well detectors going to be discussed in the later chapters are photoconductors, it is useful to know the general properties of a photoconductor. Consider a detector with surface area A_d and a thickness L . An optical flux Φ_s is incident normally upon the surface as shown in Fig. 1.7. Due to optical absorption, the intensity of the flux decreases with the penetrating depth x .

$$\Phi(x) = \Phi_s(1-r)e^{-\alpha x}, \quad (1.29)$$

where r is the surface reflection, and α is the absorption coefficient. The generating rate $G(x)$ per unit volume is

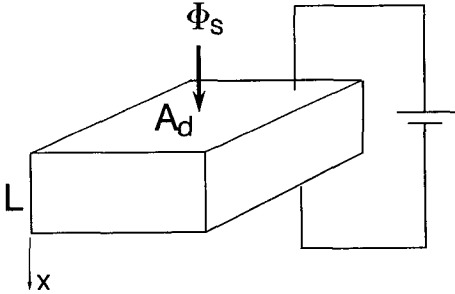


Fig. 1.7 The detector geometry.

$$G(x) = -\frac{1}{A_d} \frac{d\Phi(x)}{dx}. \quad (1.30)$$

In the steady state, the electron density $\rho(x)$ is time independent, so that

$$\frac{\partial \rho(x)}{\partial t} = G(x) - \frac{\rho(x)}{\tau} = 0, \quad (1.31)$$

where τ is the recombination lifetime of the electrons. Eq. (1.31) gives

$$\rho(x) = G(x) \tau. \quad (1.32)$$

The average photoelectron density $\bar{\rho}$ over the sample thickness is

$$\begin{aligned} \bar{\rho} &= \frac{1}{L} \int_0^L G(x) \tau dx, \\ &= \left[(1-r) \alpha \int_0^L e^{-\alpha x} dx \right] \frac{1}{A_d L} \Phi_s \tau, \\ &= \eta \frac{\Phi_s \tau}{A_d L}. \end{aligned} \quad (1.33)$$

If a voltage is applied between the top and bottom surfaces, the photocurrent i_s generated will be

$$i_s = A_d \bar{\rho} e v = (\eta \Phi_s) e \left(\frac{v \tau}{L} \right) \equiv (\eta \Phi_s) e g, \quad (1.34)$$

where v is the drift velocity of the photoelectrons, and $g = v\tau/L$ is the photoconductive gain of the photoconductor. g can be interpreted as the ratio of the electron mean free path to the sample thickness, or the ratio of photoelectron lifetime to the transit time (L/v) across the sample.

Since $\eta\Phi_s$ is the number of photoelectrons generated in the detector per second and i_s is the number of electrical charges collected at the electrical contact per second, Eq. (1.34) suggests the effective charge of each photoelectron is ge in a photoconductor, instead of the expected e . It is because each photoelectron, due to its finite lifetime, can only complete part of the circuit before recombination, which leads to a reduction of charges collected at the contact. Of course, g need not be less than one. From the definition of g , when τ is long, v is high, or L is small, while η is maintained constant, the rate of electrons collected at the contact can be larger than the rate of photoelectron generated. This situation is possible because in the derivation, the photoelectron density is assumed to be same with or without a current flow, which means that when a photoelectron leaves the sample, another electron of the same energy will be injected from the opposite contact to maintain the constant photoelectron density. One can then visualize such a phenomenon as the same photoelectron recirculating the circuit a number of times until it recombines. During its lifetime τ , a photoelectron would have left the sample ($v\tau/L = g$) times, leading to a total charges of ge being collected at the contact for each photoelectron created.

For thin detectors, additional electron recombination mechanisms at the contact layers may reduce the lifetime of the photoelectrons. Assuming the photogeneration is uniform as a function of x , in the presence of surface recombination, the spatial variation of the photoelectron density $\rho(x)$ follows

$$\frac{\partial \rho(x)}{\partial t} = D \frac{\partial^2 \rho(x)}{\partial x^2} - \frac{\rho(x)}{\tau} + G(x) = 0, \quad (1.35)$$

where D is the diffusion coefficient of the photoelectrons. Eq. (1.35) can be solved exactly, from which $\bar{\rho}$ can be obtained. In the following, however, an approximate

solution is being sought, which may be more intuitive. We look for the effective lifetime of a photoelectron in the presence of surface recombination. Considering that the detector is under illumination, and at certain time, the illumination is switched off, the transient distribution is given by

$$\frac{\partial \rho(x, t)}{\partial t} = D \frac{\partial^2 \rho(x, t)}{\partial x^2} - \frac{\rho(x, t)}{\tau} . \quad (1.36)$$

To solve Eq. (1.36), $\rho(x, t)$ is assumed of the form

$$\rho(x, t) = \rho_o \exp\left(-\frac{t}{\tau_{eff}}\right) \cos\left[\xi\left(x - \frac{L}{2}\right)\right], \quad (1.37)$$

where ρ_o and ξ are parameters to be determined, τ_{eff} is the effective lifetime. At any time t , the photoelectrons diffused from the bulk of the detector are recombined at the contacts. The boundary conditions under current continuity are

$$\begin{aligned} D \frac{\partial \rho(x)}{\partial x} &= v_s \rho(x), & \text{at } x = 0, \\ -D \frac{\partial \rho(x)}{\partial x} &= v_s \rho(x), & \text{at } x = L, \end{aligned} \quad (1.38)$$

where v_s is the surface recombination velocity. When v_s is small, substituting Eq. (1.37) into Eq. (1.38) gives $\xi^2 = 2v_s/DL$. When v_s is large, $\rho = 0$ at the contacts, which gives $\xi = \pi/L$.

On the other hand, substituting Eq. (1.37) into Eq. (1.36) gives

$$\begin{aligned} \frac{1}{\tau_{eff}} &= D \xi^2 + \frac{1}{\tau}, \\ &= \frac{2v_s}{L} + \frac{1}{\tau} \quad \text{for small } v_s, \\ &= \frac{D \pi^2}{L^2} + \frac{1}{\tau} \quad \text{for large } v_s. \end{aligned} \quad (1.39)$$

τ_{eff} at any location is decreased in the presence of surface recombination because, in

addition to the bulk recombination process, diffusion process driven by surface recombination will also reduce photoelectron density at that location. Under a steady optical power, the spatially averaged electron density $\bar{\rho}$ and hence i_s are the same as Eq. (1.32) and Eq. (1.33) respectively except that τ is replaced by τ_{eff} . For small ν_s , the approximate solution is found to be the same as the exact solution. However, when ν_s is large, the constant π^2 in Eq. (1.39) needs to be replaced by a numerical value of 12.

Since the time dependence of $i_s(t)$ is of the form

$$i_s(t) = i_o e^{-t/\tau_{eff}}. \quad (1.40)$$

The frequency response will be

$$i_s(\omega) = \int_0^\infty i_o e^{-t/\tau_{eff}} e^{-i\omega t} dt = \frac{i_o \tau}{1 + i \omega \tau_{eff}}, \quad (1.41)$$

and

$$|i_s(\omega)|^2 = \frac{i_o^2 \tau^2}{1 + \omega^2 \tau_{eff}^2}. \quad (1.42)$$

The cutoff frequency f_c of the detector, defined by $2\pi f_c \tau_{eff} = 1$, is seen to be inversely proportional to the effective lifetime of the photoelectrons, and hence the cutoff frequency and gain product of a detecting material is a constant. In future discussions, the subscript *eff* will be dropped from the symbol of the effective lifetime, understanding that the lifetime referred to is always the effective lifetime, unless stated otherwise.

The signal from a detector normalized by the incident optical power P_s is known as the responsivity R . For narrow band detector,

$$P_s = \Phi_s h \nu, \quad [W] \quad (1.43)$$

where $h\nu$ is the average photon energy. R is then given by

$$R = \eta \frac{e}{h \nu} g. \quad [A/W] \quad (1.44)$$

1.3.2 Noise in a photoconductor

Previously, we discussed the noise of a detector under the assumption that all the carriers in the detector are generated optically, whether they are from the target or from the background of a scene. For a photoconductor, however, there are additional mechanisms that can increase the noise level. Although the noise associated with each physical mechanism generally has a specific name, the basic sources of noise inevitably can be traced to two different types of randomness. One is the fluctuation in the velocity of the carriers, the associated noise is referred to as Johnson noise. Another is the fluctuation in the number of carriers. As discussed before, the random nature of the quantum optical emission process of the light source and the absorption process of the detector can cause fluctuation in the carrier density. In addition, the thermionic emission process in a photoconductor will also increase the mobile carrier density and hence its statistical fluctuation. The noise associated with the generation of the mobile carriers is called generation noise. In a photoconductor, the random recombination process of mobile carriers also contributes to fluctuation of carrier density and hence increases noise. The generation-recombination (g-r) noise then collectively describe the noise caused by the fluctuation in carrier density of a photoconductor.

Other than these noise components, there are other physical processes in a photoconductor that can cause noise. For example, the presence of impurity states can cause fluctuation in both mobile and immobile electron density, with a characteristic frequency for each impurity state. The combination of different frequency response is thought to be the source of the $1/f$ noise. Another noise source is the presence of tunneling current or leakage current of the otherwise immobile electrons. Since the carriers of the tunneling current is very different in energy than that generated optically or thermally, they have a different gain value, and hence the g-r noise of the tunneling current should be treated separately. In the present general discussion, we ignore these nonideal current fluctuation, and it will be discussed in detail in later chapters.

For Johnson noise, we simply state the usual result, which is

$$i_n = \sqrt{\frac{4 k T B}{\mathfrak{R}}}, \quad (1.45)$$

where \mathfrak{R} is the resistance of the detector, and $B = 1/(2\tau_d)$ (see section 12.2) is the noise

bandwidth of an integrating filter.

For g - r noise, we first observe from Eq. (1.34) that for every second, there are $\bar{n} = \eta \Phi_s$ light absorption events, and each event produces a charge of ge . This statement is different from saying that there are $\eta \Phi_s g$ electrons collected per second and each electron has a charge of e . It is because after each photon absorption, the subsequent collections of g electrons are not independent events. Therefore, following Eq. (1.22),

$$i_n^2 = \frac{g^2 e^2}{\tau_d^2} \bar{n} = \frac{g e}{\tau_d} I = 2 g e I B . \quad (1.46)$$

Here, I is the total current generated by either optical excitation or by thermal excitation. In Eq. (1.46), the value of g is assumed to be a constant. However, in the presence of random recombination process, g is an average value. It is the value of the gain when an electron recombines at time τ , the average lifetime of a photoelectron or a thermal electron. If a particular electron recombine at time t , the effective charge will be $(gt/\tau)e$. The probability $p(t)$ of an electron to recombine at time t is

$$p(t) = \frac{1}{\tau} e^{-t/\tau} . \quad (1.47)$$

The contribution to the current flow by the electrons recombined between t to $t + dt$ is

$$dI = \left(\frac{t}{\tau} \right) I p(t) dt . \quad (1.48)$$

The total noise current caused by the photoelectrons and the thermal electrons is

$$\begin{aligned} i_n^2 &= \int_0^\infty 2B \left(\frac{gt}{\tau} e \right) \left(\frac{t}{\tau} I \right) p(t) dt , \\ &= 2 e g I B \int_0^\infty \left(\frac{t^2}{\tau^3} \right) e^{-t/\tau} dt , \\ &= 4 e g I B . \end{aligned} \quad (1.49)$$

Therefore, comparing Eq. (1.49) with Eq. (1.46), the fluctuation of g due to the recombination process increases the noise power by a factor of two.

Since I is given by

$$I = i_s + i_b + i_{th} = \eta g e \left(\Phi_s + \Phi_b + \frac{i_{th}}{\eta g e} \right), \quad (1.50)$$

where i_s , i_b and i_{th} are the target generated, background generated and thermally generated current, the signal to noise level of a photoconductor is

$$\left(\frac{S}{N} \right)_p = \frac{i_s^2}{i_n^2} = \frac{\eta}{4B} \frac{\Phi_s^2}{\Phi_s + \Phi_b + \frac{i_{th}}{\eta g e}}. \quad (1.51)$$

Here, we have not included the Johnson noise, since it is generally much less than the g - r noise at a finite bias. When the detection is signal limited, the noise equivalent flux Φ_{SL} is

$$\Phi_{SL} = \frac{4B}{\eta} = \frac{2}{\eta \tau_d}. \quad (1.52)$$

Comparing Eq. (1.52) and Eq. (1.25), Φ_{SL} for a photoconductor is a factor of two larger than a detector with a constant g ($= 1$). In the present case, it is necessary to wait for two absorption events and collect $2g$ photoelectrons in each measurement to produce a $(S/N)_p$ of unity. When the detection is background limited,

$$\Phi_{BL} = \sqrt{\frac{4B}{\eta} \Phi_b} = \sqrt{\Phi_{SL} \Phi_b}, \quad (1.53)$$

where Φ_{SL} is defined in Eq. (1.52). Comparing Eq. (1.53) with Eq. (1.28), Φ_{SL} for a photoconductor is a factor of $\sqrt{2}$ larger than a detector with a constant g . When it is thermionic emission current limited,

$$\Phi_{THL} = \sqrt{\frac{4B}{\eta} \frac{i_{th}}{\eta e g}} = \sqrt{\Phi_{SL} \frac{i_{th}}{\eta e g}} \quad (1.54)$$

For each noise equivalent flux, one can also define the noise equivalent power NEP ,

which is simply the noise equivalent flux times the average photon energy.

Notice that NEP in both the background limited case and the thermionic emission case is directly proportional to $\sqrt{(A_d B)}$, which is unrelated to the material properties. Therefore, it is more convenient to compare different detectors with the quantity $\sqrt{(A_d B)}/NEP$, defined as the detectivity D^* . A larger D^* means a smaller NEP and hence a more sensitive detector. In the background limited case,

$$D_{BL}^* = \frac{\sqrt{\eta}}{2 h \nu} \frac{1}{\sqrt{\Phi_b/A_d}} = \frac{\sqrt{\eta}}{2 h \nu \sin \theta} \frac{1}{\sqrt{M(T_b, \lambda_1, \lambda_2)}}, \quad (1.55)$$

where θ is the half-cone angle, and $M(T_b, \lambda_1, \lambda_2)$ is the exitance given in Eq. (1.6) for the background temperature of T_b . Since the only material parameter in Eq. (1.55) is the quantum efficiency η , D_{BL}^* can be increased only by increasing η . On the other hand, if the detection is thermionic emission current limited,

$$D_{THL}^* = \frac{\eta}{2} \sqrt{\frac{e g}{J_{th}}}, \quad (1.56)$$

where J_{th} is the thermionic emission current density. A larger D_{THL}^* means a larger η , a larger g and a smaller thermionic current.

D^* is a useful and convenient figure of merit in comparing different detectors. It concisely summarizes the effects of η , g and J_{th} of a detector in its sensitivity. However, the value of D^* alone may not convey sufficient information for detector evaluation. Different combinations of detector parameters can yield the same D^* , but not all of the them are suitable for a particular application. Moreover, it does not cover other factors that are also important in infrared detection. For example, it makes no reference on the uniformity and the quality of the detector material, also it does not indicate the impedance, the speed, the response linearity, and the current level of the detector. In modern high resolution thermal imaging, these factors are equally important as the value of D^* .

Fig.1.8 shows D_{BL}^* for two ideal photoconductors sensitive in 3 to 5 μm and 8 to 10 μm respectively. η is assumed to be 1 in both specific spectral regions. The half-cone angle θ is assumed to be 14° and 90° respectively. $M(T_b, \lambda_1, \lambda_2)$ in Eq. (1.55) is given by Eq. (1.6). At $T_b = 300$ K, D_{BL}^* at 4 μm band is $3.62 \times 10^{11} \text{ cm}\sqrt{\text{Hz/W}}$, which

is nearly twice as large as the D^*_{BL} ($= 1.79 \times 10^{11}$ cm $\sqrt{\text{Hz/W}}$) at 9 μm band.

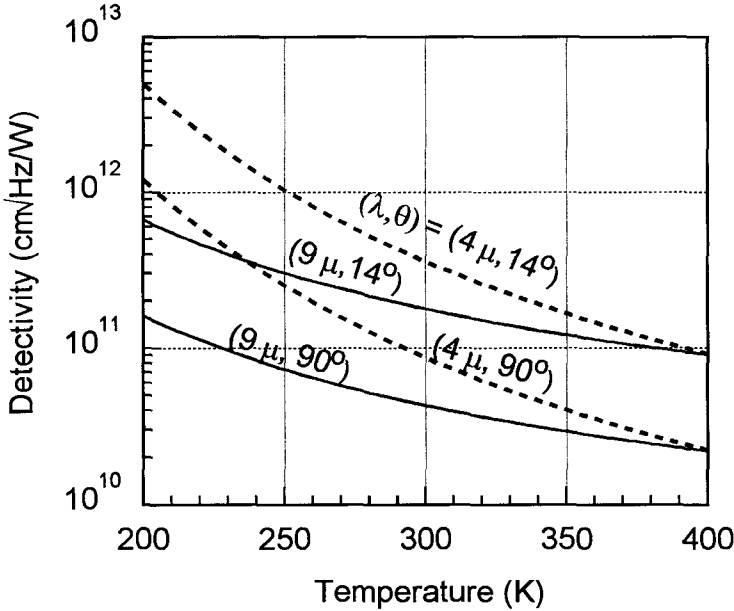


Fig. 1.8 The D^* of an ideal photoconductor in two wavelength bands.

At lower temperature, the difference is even higher. The smaller D^* occurred at the 9 μm band indicates the larger noise level in this band because of the more intense background radiation. If a target emits same level of radiation in both bands, then it is more advantageous to detect the object at the shorter wavelength bands. However, if the object has a similar temperature as the background, then the reverse is true. It is because the detection is not only dependent on the NEP but also on the signal level of the target, which is stronger in the 9 μm band below $T = 643$ K. In fact, substituting the expression of D^* in both the background limited case and the thermionic emission limited case into Eq. (1.51) yields

$$\left(\frac{S}{N}\right)_p = (D^* E_s)^2 \frac{A_d}{B}, \quad (1.57)$$

where E_s is the average irradiance of the source, and is given by

$$E_s = \frac{P_s}{A_d} = L_s h \nu \Omega_s = \pi L_s h \nu \sin^2 \theta_s = M_s h \nu \sin^2 \theta, \quad (1.58)$$

where Ω_s is the projected solid angle of the source, and L_s is the radiance of the source in the respective band. M_s is the shorthand for exitance $M(T, \lambda_1, \lambda_2)$ given by Eq. (1.6). The ratio of $(S/N)_p$ between these two bands for the background limited case is

$$\frac{(S/N)_{9\mu m}}{(S/N)_{4\mu m}} = \left(\frac{D_{BL}^*(9\mu m) M(T_s, 8\mu m, 10\mu m) h \nu_{9\mu m}}{D_{BL}^*(4\mu m) M(T_s, 3\mu m, 5\mu m) h \nu_{4\mu m}} \right)^2 = 21, \quad (1.59)$$

where the source temperature of $T_s = 300$ K have been assumed. Even though the D_{BL}^* of an ideal detector and the contrast of the scene are both a factor of two lower in the $9\mu m$ band, the signal to noise level can be 21 times higher, depending on the source temperature. Therefore, it is more likely to obtain a noise free thermal image in the $9\mu m$ band. Notice that in the above example, T_b is assumed to be the same as T_s . One can actually treat the background scene as the source, and the detection is signal limited. Although Φ_{SL} is directly proportional to B and is independent on A_d , and hence D^* cannot be defined in this case, the ratio of the $(S/N)_p$ between the two bands can be shown to be the same as that of Eq. (1.59).

Other than NEP and D^* , another useful figure of merit is the noise equivalent temperature difference $NE\Delta T$, which is defined as the temperature difference of the scene which produces a power difference equal to NEP of the detector. It is the minimum temperature difference of the scene that a detector can detect. By definition,

$$NE\Delta T = \frac{NEP}{dP_b/dT} = \sqrt{\frac{B}{A_d}} \frac{1}{D^* \sin^2 \theta} \frac{1}{k M_b} \left(\frac{k T_b}{h \nu} \right)^2. \quad (1.60)$$

When it is background limited, substituting Eq. (1.55) into Eq. (1.60) leads to

$$(NE\Delta T)_{BL} = \frac{\sqrt{2}}{C} \frac{1}{\sqrt{\eta} \Phi_b \tau_d} = \frac{\sqrt{2}}{C} \frac{1}{\sqrt{N_e/g}}, \quad (1.61)$$

where C is the contrast defined in Eq. (1.8), Φ_b is the optical flux on the detector, τ_d is

the time duration or the integration time of the measurement, N_e is the number of background photoelectrons collected in τ_d , and g is the photoconductive gain. From Eq. (1.61), although the contrast of the scene at 9 μm band is less than that at 4 μm band, the much larger photon flux at the 9 μm band over compensates the lower contrast, and the resulting $NE\Delta T$ of a 300 K scene at the 9 μm band is 1.84 times less than that at the 4 μm band, assuming the same detector parameters in both bands. The smaller resolved temperature difference is due to a better signal to noise level despite of a lower contrast.